Dielectric and calorimetric signatures of chain orientation in strong and tough ultrafine electrospun polyacrylonitrile

Steven Araujo, Nicolas Delpouve, Laurent Delbreilh, Dimitry Papkov, Yuris Dzenis, Eric Dargent

Dielectric and calorimetric signatures of chain orientation in strong and tough ultrafine electrospun polyacrylonitrile

Steven Araujo[a], Nicolas Delpouve[a*], Laurent Delbreilh[a], Dimitry Papkov[b,c], Yuris Dzenis[b,c], Eric Dargent[a]

[a] Normandie Univ, UNIROUEN Normandie, INSA Rouen, CNRS, Groupe de Physique des Matériaux, 76000 Rouen, France

[b] Department of Mechanical and Materials Engineering, University of Nebraska–Lincoln, Lincoln, NE 68588-0526

[c] Nebraska Center for Materials and Nanoscience, University of Nebraska–Lincoln, Lincoln, NE 68588-0298

* Corresponding author: Nicolas Delpouve

Normandie Univ, UNIROUEN Normandie, INSA Rouen, CNRS, Groupe de Physique des Matériaux, 76000 Rouen, France

Tel: +33 (0)232955165 / Fax: +33 (0)232955082 ; Email: nicolas.delpouve1@univ–rouen.fr

Abstract

Ultrafine diameter fibers of polyacrylonitrile (PAN), obtained from electrospinning, have huge potential for structural applications since they exhibit an unusual combination of strength and toughness. However, the difficulty to characterize their supramolecular architecture limits their production at the industrial scale. In this work, the glass transition of electrospun nanofiber mats of PAN was investigated by means of thermal analysis techniques. Modulated temperature differential scanning calorimetry (MT–DSC) and dielectric relaxation spectroscopy (DRS) were used, and relaxation parameters characteristic of the glass transition were obtained. Reduction in average fiber diameter resulted in broadening of the glass transition and a shift of its midpoint to higher temperatures as observed by MT–DSC, revealing additional level of constraints in the amorphous phase. The DRS curves, obtained above the calorimetric signature of the glass transition, superimpose independently on the fiber diameter. This result, which contrasts with MT–DSC observations, shows that the

constraint of mobility evidenced at the glass transition, is suppressed when driving the fiber mat to higher temperatures. The dielectric strength increases with temperature, revealing an increase in the density of dipoles participating to the relaxation dynamics. This result, commonly attributed to the progressive mobilization of initially constrained amorphous phase, supports the hypothesis that electrospinning process induces higher level of polymer chain orientation at small fiber diameters, which fades away when crossing the glass transition. The orientation impacts the temperature dependence of the relaxation time close to the glass transition, as it shows higher deviation from Arrhenius behavior with the decrease of the fiber diameter. This leads to an increase of the fragility index which comes in opposition to the decrease in the cooperativity length, estimated from the temperature fluctuation approach of the cooperative rearranging region (CRR) concept. To explain this result, both volume and thermal contributions of the fragility index have been calculated, and a strong increase in the thermal contribution has been observed for the most oriented material. This result is interpreted as a signature of an increase in the polymer chain rigidity.

INTRODUCTION

Electrospinning is a process which allows creating continuous micro– or nanofibers by jetting polymer solution in high electric field [1–10]. Due to the growing interest in the fabrication of continuous nanofibers for structural and functional applications, electrospinning was used in different fields such as tissue engineering [4,11], medical [12], filtration [6,13], food industry [14] and opto–electronics [15]. Fibers obtained by electrospinning can exhibit outstanding mechanical properties, such as combined strength and toughness, when their diameter is less than 250 nm [16]. To explain this result, it was hypothesized that electrospinning can generate high level of orientation while preserving low degree of crystallinity [16]. Indeed, the macromolecular chains undergo both electrical and mechanical stretching during electrospinning [1]. On the other hand, the crystalline growth occurs in a confined environment which can slow down the crystallization kinetics [17]. In addition, fast solvent evaporation may hinder the crystallization process [18]. As a result, the microstructure generated by electrospinning is complex, with the possible coexistence of crystalline and amorphous phases, as well as mesophase [19]. Mesophase is defined as an intermediate order structure which is a precursor to crystallization [20–22]. Ma *et al.* [23] investigated the formation of mesophase in electrospun polylactide. They show [23] that mesophase behaves

similarly to rigid amorphous fraction (RAF), i.e., the part of the amorphous phase, resulting from the coupling between crystal and amorphous phases, which does not relax at the glass transition [24–26].

The possibility to process nanofibers that are both strong and tough is very appealing. To reach this objective, the microstructure in the nanofibers should be perfectly controlled. The evaluation of orientation is particularly critical since the polymer chain alignment is one probable needed condition for the nanofiber to exhibit high values of modulus, true strength, and toughness, as previously reported [16]. Despite the interest to characterize polymer chain orientation in electrospun fibers, access to such information is highly challenging [27]. Relevant spectroscopic techniques exhibit significant artefacts due to light interaction with sub–wavelength diameter fibers, exhibiting high surface curvature [28]. In addition analysis of individual fibers requires designing new experimental protocols. Consequently, most of the studies are currently carried out on nanofiber mats. The question of the quantification of polymer chain orientation in nanofibers has been reviewed recently [29]. Various techniques, including X–Ray diffraction, Polarized Fourier Transform, infrared spectroscopy, thermal analyses, NMR, selected area electron diffraction, polarized optical light spectroscopy, polarized Raman spectroscopy, and also emerging techniques for evaluation of orientation, were investigated. Although some techniques are promising for quantification of orientation, most of them are restricted to the analysis of the orientation in the crystalline phase [29]. However superfine nanofibers are characterized by their low crystallinity. Therefore the interrogation of the amorphous phase is crucial and it is of interest to propose new approaches to characterize polymer chain alignment in electrospun systems. The goal of this study is to investigate whether the orientation of the amorphous phase in the electrospun nanofibers could be tracked from thermal analysis. To do so, characterization of polyacrylonitrile (PAN) nanofiber mats has been performed by both modulated temperature differential scanning calorimetry (MT–DSC) and dielectric relaxation spectroscopy (DRS). In PAN, degradation occurs before melting. Thus the analysis of the calorimetric data is jeopardized by the degradation which modifies or suppresses the response of the sample during the melting. In this context it becomes difficult to assess properties regarding the crystalline phase of PAN from DSC curves. Only the amorphous state can be safely interrogated from usual thermal analysis protocols. Our idea is to investigate whether the glass transition signature in nanofiber mats changes as a function of the average fiber diameter. The cooperative rearranging region (CRR) concept introduced by Adam and Gibbs [30] has been applied at the glass transition of PAN. A CRR is defined [30] as a subsystem which can rearrange its

configuration into another, independently of its environment upon a sufficient thermal fluctuation. Each subvolume can be then considered as a thermodynamic system in metastable equilibrium with fluctuating variables [30]. Calculating the CRR size when the glass transition occurs in restricted volume, i.e., confined environment at the nanoscale, has been the object of previous studies [31–33]. A decrease of the CRR size has been reported when the amorphous phase is confined between the layers of organophilic clay [31], in multi nano–layer polymer films [32], and by crystals [33]. Furthermore, many investigations on drawn films also evidenced a decrease in the cooperativity length [34–38] as well as anisotropy in the CRR size [38]. Monnier *et al.* [39] investigated the CRR size in electrospun fibers of polylactide. They showed that the very early stage of orientation of electrospinning is characterized by the cohesive role of mesophase which leads to a slight increase in the CRR size [39]. Cho et al. [40] showed by employing Adam-Gibbs theory that the fast interface dynamics of polymer fibers should influence the cooperative motion of monomers. Furthermore, the calculation of CRR size has recently be applied to new biobased polymers [41].

In this work the relaxation dynamics of PAN nanofibers mats are investigated at the calorimetric glass transition from MT–DSC, and in the liquid state from DRS. The temperature dependence of the relaxation time is obtained from DRS, and the degree of deviation from Arrhenius behaviour, i.e., the fragility index [42] is calculated. Since the improvement of mechanical properties, essentially attributed to the high orientation in the amorphous phase linked to low degree of crystallinity, is observed for diameter less than 250 nm, the average diameter of the PAN fiber in the mat goes down to 232 nm.

EXPERIMENTAL

Materials

PAN fibers were electrospun at ambient conditions from PAN (Pfaltz and Bauer, Inc.®; cat# P21470, M_W = 150 000 g/mol in average) solutions in N,N–dimethylformamide (DMF) (Sigma–Aldrich®; cat# 271012) in a 1 mL syringe using a 20 gauge needle and a feed rate equal to 0.6 mL/h. Fibers were collected on a stationary target covered with aluminium foil. The applied voltage was 12 kV; the distance between the spinneret and collector was 20 cm. The samples were electrospun from 8, 10, and 12 wt% of PAN in DMF.

Scanning electron microscopy (SEM)

Nanofiber diameter was examined by scanning electron microscopy (SEM) in an environmental apparatus (Quanta 200 FEG from FEI®) with no coating and no additional preparations. Several images of each mat were taken at different locations. Nanofiber diameters were measured for at least 200 fibers in each sample using ImageJ® software, average diameter was calculated, and a histogram was constructed.

Modulated temperature differential scanning calorimetry (MT–DSC)

Experiments were performed on a DSC Q100 Thermal Analysis® instrument. The samples, cut from fiber mats, then folded, were about 2 mg, encapsulated in Tzero® DSC aluminum alloy pans, and disposed to recover the surface of the pan in contact with the thermal sensor. Calibration in temperature was carried out using standards of indium and benzophenone. Calibration in energy was carried out using standard values of indium. The specific heat capacity for each sample was measured using sapphire as a reference. The modulation parameters were chosen to obtain a clear view of the glass transition (oscillation amplitude of 2.5 K, oscillation period of 100 s, and heating rate of 1 $K.min^{-1}$). The furnace was permanently swept by nitrogen flow (50 mL/min).

Broadband Dielectric Spectroscopy (DRS)

Dielectric relaxation spectra were measured with an Alpha Analyzer from Novocontrol® (frequency interval: 10^{-1}—10^{6} Hz). A portion of the mat was cut and placed between parallel electrodes, and the temperature was regulated through a heated flow of nitrogen gas, by means of a Quatro Cryosystem®, from 343 K to 473 K. The sample geometry was ranged from 80 to 100 μm thick and 20 mm diameter (upper electrode) for each sample. The thickness was measured when the nanofiber mat was placed between the electrodes. The complex permittivity ε^* is calculated from:

$$\varepsilon^*(\omega) = \varepsilon' - i\varepsilon'' = \frac{-i}{\omega Z^*(\omega) C_0} \quad (1)$$

Where Z* = U* / I* is the impedance calculated from the Novocontrol system, U^* is the applied voltage and I^* the measured current, ε' and ε'' are the real and imaginary parts of ε^*, i is the unit imaginary number, $\omega (=2\pi f)$ is the angular pulsation and f the frequency, C_0 is the ideal empty cell capacity:

$$C_0 = \varepsilon_0 \frac{\pi D^2}{4d} \quad (2)$$

Where ε_0 is the vacuum permittivity, D is the diameter of the capacitor (upper electrode) and d is the thickness of the sample.

The conductivity σ^* of the material is calculated from the permittivity:

$$\sigma^* = \sigma' - i\sigma'' = i2\pi f \varepsilon_0 (\varepsilon^* - 1) \quad (3)$$

To analyze dielectric relaxation curves, the imaginary part of the permittivity has been fitted thanks to Havriliak–Negami (HN) complex function [43]. Grafitylab software was used to fit the experimental data using the least squares method. The correlation coefficient of the Havriliak-Negami fits was higher than 0.99 for the whole sample series. The relaxation times were extracted isothermally using a HN contribution and a conductivity term.

$$\varepsilon^*(\omega) = -i\left(\frac{\sigma}{\omega\varepsilon_0}\right)^n + \sum_k \frac{\Delta\varepsilon_k}{[1+(i\omega\tau_k)^{\alpha_k}]^{\beta_k}} + \varepsilon_\infty \quad (4)$$

Where k is the number of contributions for the fitting procedure (equal to 1 in the present study), n is a fitting parameter related to the conductivity slope, $\Delta\varepsilon$ is the dielectric strength, τ is the relaxation time, and α and β are the broadening and asymmetric shape factors. ε_∞ is the permittivity at high frequency of the relaxation process, with $\Delta\varepsilon = \varepsilon_S - \varepsilon_\infty$, where ε_S is the permittivity at low frequency (static). The errors associated to the fitting procedure are estimated about 5% for α and β and 3% for σ, n, τ and $\Delta\varepsilon$.

RESULTS AND DISCUSSION

SEM pictures of the electrospun fibers are given in Figure 1. For all compositions, the fiber shape is globally homogeneous and the majority of the fibers do not show any beading effect. For 8, 10, and 12 wt% of PAN in DMF, the average diameter of fibers in the mats are 232 nm (Fig. 1a), 451 nm (Fig. 1b), and 785 nm (Fig. 1c), respectively. In the following sections, the samples are named as PAN_232, PAN_451, and PAN_785 accordingly.

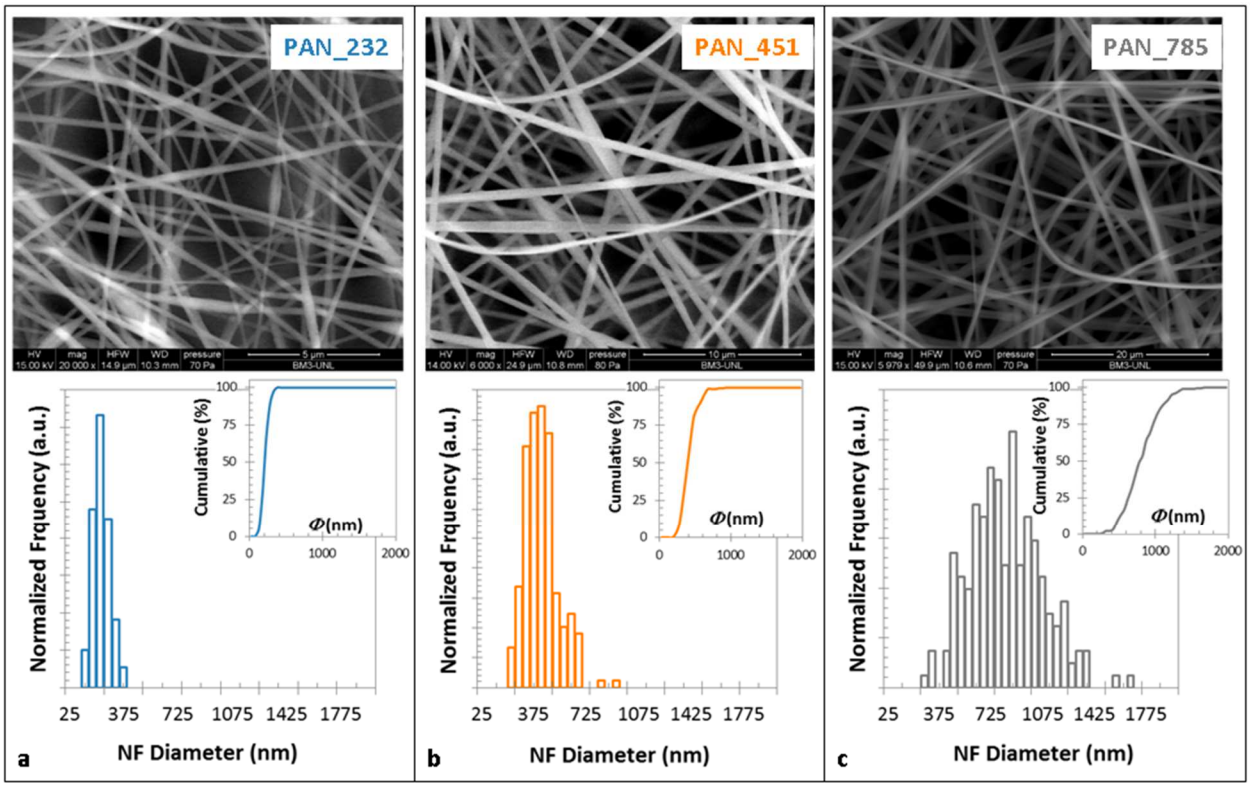

Figure 1. SEM pictures along with the fiber diameter distribution of as–spun solutions containing 8 **(a)**, 10 **(b)**, and 12 **(c)** wt% of PAN in DMF respectively. Samples are named PAN_*x*, where *x* is the fiber average diameter in the PAN.

The diameter is less dispersed when decreasing the concentration of polymer in solvent. PAN_785 exhibits the widest dispersion in the fiber diameter, whereas the diameter profile is the narrowest for PAN_232. Besides, the fiber diameter distribution of PAN_232 does not extend beyond 375 nm, whereas 375 nm is close to the minimum fiber diameter in PAN_785. Therefore the role of fiber size on both thermal characteristics and relaxation properties can be reliably investigated through the analysis of the three nanofiber mats. From the average heat flow curves recorded from MT–DSC (shown in Supporting Information Figure SI.1), the calorimetric signature of the glass transition is indiscernible since it is covered by parasitic thermal events. A clear view of the glass transition can however be obtained by applying the complete deconvolution procedure, suggested by Reading [44], to obtain the in–phase component *C'* of the complex heat capacity. MT–DSC recorded variations of *C'* in the glass transition domain are presented in Figure 2a. Characteristic parameters obtained from the glass transition investigation are given in Table 1.

Table 1. Relaxation parameters obtained from MT–DSC and DRS for PAN_232, PAN_451, and PAN_785. Fragility values are given with an uncertainty of 10 %. m_V and (m - m_V) are calculated for α_T/κ = 1.5 MPa / K.

	MT–DSC				DRS		
	ΔCp (J g^{-1} K^{-1})	$T_{g\ mid}$ (K)	δT (K)	$\xi_{T\alpha}$ (nm)	m	m_V	m - m_V
PAN_232	0.40 ± 0.04	360 ± 1	6.2 ± 0.2	1.7 ± 0.2	133 ± 14	124 ± 13	9 ± 1
PAN_451	0.27 ± 0.04	354 ± 1	4.5 ± 0.2	1.9 ± 0.2	106 ± 11	93 ± 10	13 ± 2
PAN_785	0.30 ± 0.04	351 ± 1	4.0 ± 0.2	2.2 ± 0.2	100 ± 10	81 ± 9	19 ± 2

The curves have been shifted to coincide at 333 K with the solid heat capacity values given by Gaur *et al.* [45]. The corresponding equation of solid heat capacity that was reported is Cp = exp[0.222649 (ln T)^3 – 3.36593 (ln T)^2 + 17.6347 (ln T) – 28.1638] J mol^{-1} K^{-1}. This procedure can be applied since the solid heat capacity is expected to be largely independent on the microstructure [46]. This means that, although the degree of crystallinity and the degree of orientation should be different between samples, we assume the solid heat capacity to remain invariant. It is helpful when the heat capacity variation with temperature has to be accurately known, as for the CRR calculation. The glass transition temperature measured at midpoint $T_{g\ mid}$ is shifted towards higher temperature (from 351 to 360K) with the decrease of the fiber diameter. Furthermore, the glass transition significantly broadens. According to Hempel *et al.* [47], the temperature fluctuation δT associated with the main relaxation process (α–relaxation) reflects the heterogeneity in the amorphous phase dynamics. δT was estimated by fitting dC'/dT (shown in Figure 2b) with a Gaussian peak shape and determining its standard deviation. δT increases from 4.0 K for PAN_785 to 6.2 K for PAN_232. Many studies report an enlargement of the glass transition, i.e., an increase of δT, when the amorphous phase mobility is hampered by geometrical confinement [31–32], crystalline growth [33,36], or orientation [34–38]. From Figure 2a, one can observe that the heat capacity step at the glass transition is significantly higher for PAN_232 (ΔCp = 0.40 J g^{-}1 K^{-1} versus approximately 0.30 J g^{-}1 K^{-1} for the two other materials). This indicates that the relative content of amorphous phase relaxing at the glass transition increases with the decrease of the average fiber diameter. This means that the broadening and the shift of the glass transition for PAN_232 are not related to higher crystallinity content. This result is however consistent with

previous work reporting that the reduced diameter fibers have less crystallinity but improved chain orientation [16]. Similar results were obtained by characterizing electrospun PAN fibers from several techniques including X–Ray diffraction, Infrared and Raman spectroscopy [29].

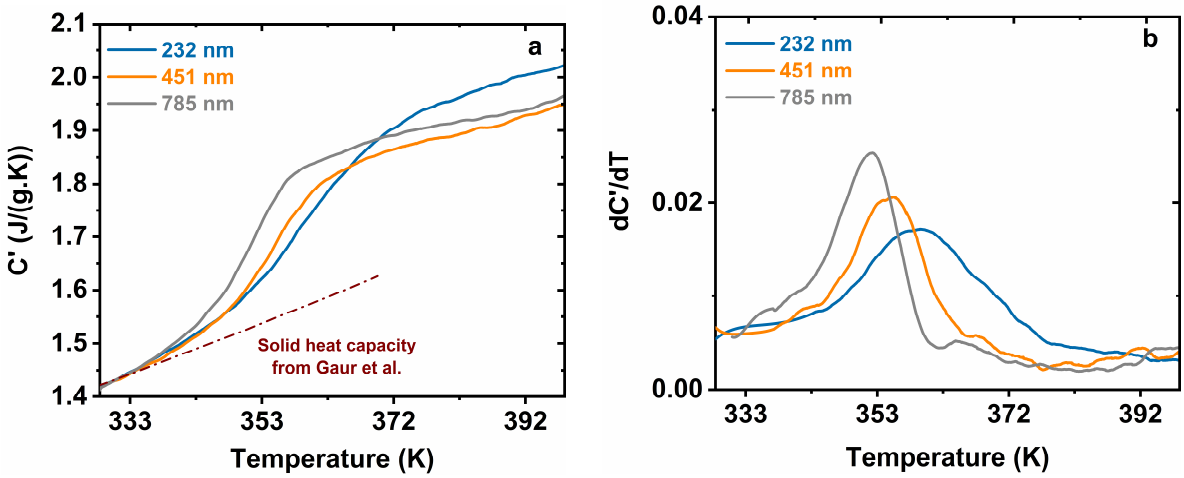

Figure 2. (a) MT–DSC in–phase (*C'*) component of the complex heat capacity and **(b)** its derivative *dC'/dT* versus temperature for PAN_232, PAN_451, and PAN_785.

As constraint slackening in polymer chains is expected to occur above the calorimetric glass transition [48], severely impacting the amorphous phase orientation, it is interesting to extend the range of investigation of the relaxation process to higher temperatures. The range of solicitation frequency accessible from DRS experiments allows investigating the molecular mobility far above the calorimetric glass transition, as the glass transition dielectric signature (segmental relaxation) is detected at higher temperature for higher frequency. An example of the detection of the segmental relaxation as a function of temperature and frequency is given for PAN_785 in Supporting Information (Figure SI.2). For all systems, it has been obtained between 378 and 443 K. It shows that the segmental relaxation signature shifts towards lower temperatures when decreasing the frequency from 10^6 to 10^2 Hz. The frequency domain investigated has been limited by conductivity phenomena. From these curves the permittivity has been analyzed.

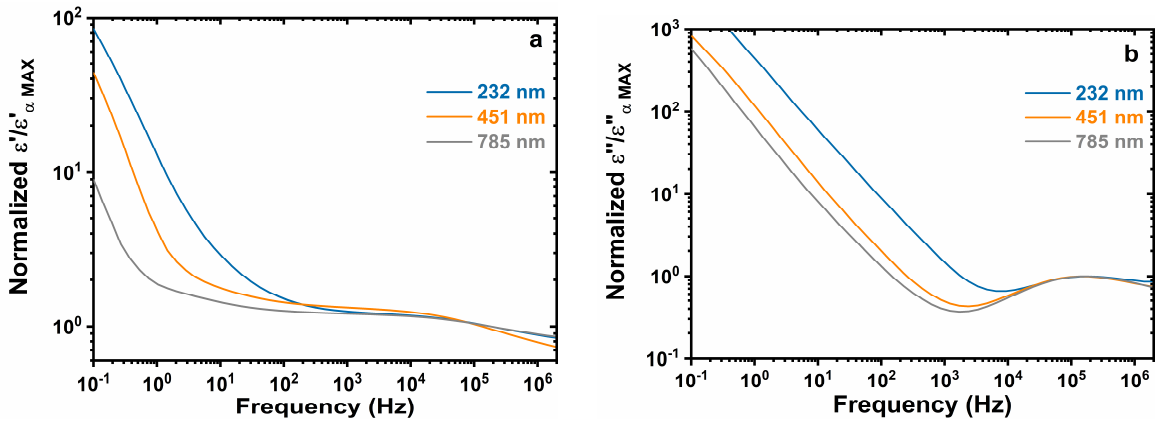

Figure 3. Real **(a)** and imaginary **(b)** parts of the complex dielectric permittivity recorded at 419 K from DRS for PAN_232, PAN_451, and PAN_785. Data have been normalized to the relaxation maximum response.

One concern for the analysis of the permittivity results is that PAN mats between parallel electrodes are not bulky materials; instead they contain a certain volume of non–controlled air (nanofibers + air between nanofibers). The real part of the permittivity of air, equal to 1, is different from the one of PAN bulk material or fiber alone. Thus, even knowing the perfect thickness of the NF mats, the measurement will not provide the accurate permittivity value of the PAN fiber alone. Electromagnetic mixing models may help to calculate the average permittivity of the two–phase material. However, the exact amount of air in the system is not known. Consequently, a normalization of the permittivity was performed to compare the shape and position of the peak maximum of the α–relaxation, i.e., real and imaginary part of the permittivity were divided by the value of ε' and ε'' at the related α–relaxation time (at 419K). This leads to $\varepsilon''/\varepsilon''_{max} = 1$ for the relaxation time corresponding to the maximum response associated with the dielectric manifestation of the glass transition. Therefore, both real and imaginary parts of the complex dielectric permittivity recorded at 419 K (random choice in the investigated temperature range) are presented after normalization in Figure 3a and Figure 3b respectively (raw data are provided in Supporting Information Figure SI.3). Nevertheless, according to Figure 3b there is no significant change in the position of the maximum (refer to Supporting Information Figure SI.3 for cross comparison between curves). At low frequencies, conductivity phenomena are superimposed to the relaxation. One can notice that the observation of relaxation is extended to 10^3 Hz for the fiber mats with largest diameter nanofibers, whereas it is restricted by conductivity to high frequencies (10^4 to 10^6 Hz) for PAN_232, which also exhibits the highest conductivity values. Figure 4 depicts the real (a) and imaginary (b) parts of the conductivity. It can be seen that the DC plateau

corresponding to the nearly linear behavior of the real part of the conductivity, increases when the fiber diameter decreases which reveals the higher conductive character when decreasing the fiber diameter. These results are consistent with the study of Zhang and Rutledge [49], which reports that the conductivity of polyaniline fibers increase by solid state drawing which both increases orientation, and decreases the average diameter. The increase in the real part of the permittivity is most likely related to the undesirable effect of electrode polarization which is observable in Figure 4b by the change of slope in the imaginary part of the conductivity [50]. It can be seen in Fig 3 and Fig 4 that the deviation (in frequency) from AC regime in both real and imaginary part of the conductivity coincide with the increase in the imaginary and real part of the permittivity respectively, related respectively to the conductivity of the material and the parasite electrode polarization effect.

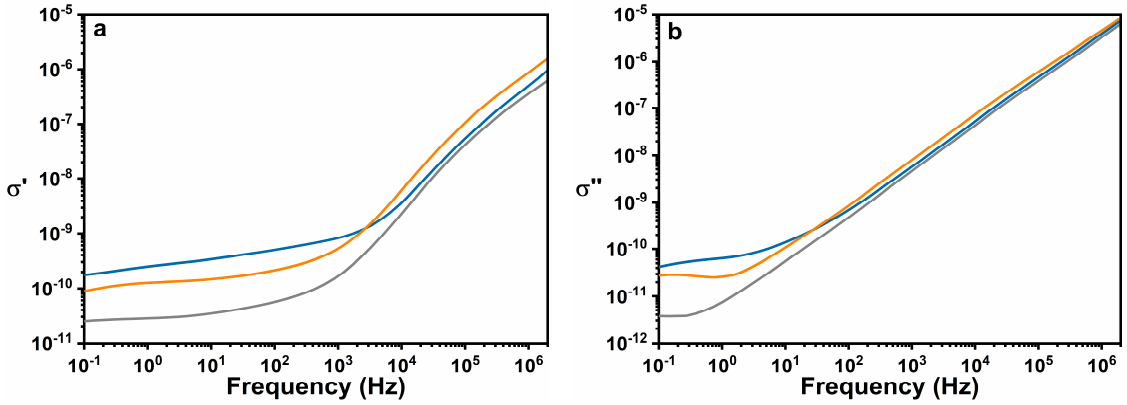

Figure 4. Real (a) and imaginary (b) parts of the conductivity as a function of frequency at 146°C for PAN_231, PAN_451 and PAN_785.

More information related to the mobility in constrained amorphous phase can be obtained from the variations of the dielectric strength $\Delta\varepsilon$. The values of $\Delta\varepsilon$ were obtained from the HN analysis of raw data. An example of Havriliak–Negami fitting is given in Figure 5. It can be seen that the experimental points are well fitted with a conductivity term and a HN contribution. Examples of fitting parameters related to the conductivity term are given in Table SI.1 of the Supporting Information. Figure 6 displays the fitting parameters α and β obtained from Havriliak–Negami equation. For the lowest accessible temperatures, about 40 K above the calorimetric glass transition, the fitting parameters are quite different, revealing potential structural differences between samples. On the other hand, for the highest temperatures, the samples exhibit the same fitting parameters (close to 0.7 for α and to 0.45

for β) as the relaxation shape starts to merge for each sample to finally have the same shape at very high temperature.

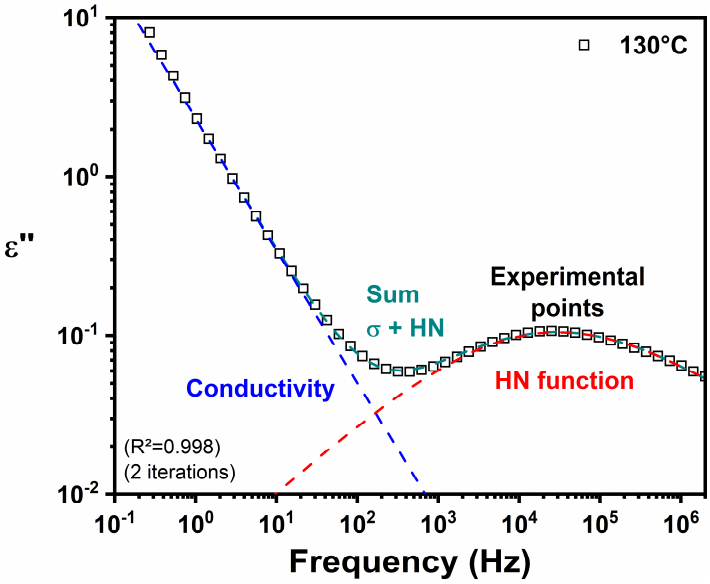

Figure 5. Example of the fitting procedure with a conductivity term and a HN contribution performed for PAN_785 at 130°C. Empty squares are the experimental points, red dash line is the HN function, blue dash line is the conductivity term and dark cyan dash line is the sum of the two contributions. The obtained correlation coefficient is equal to 0.998 after 2 iterations.

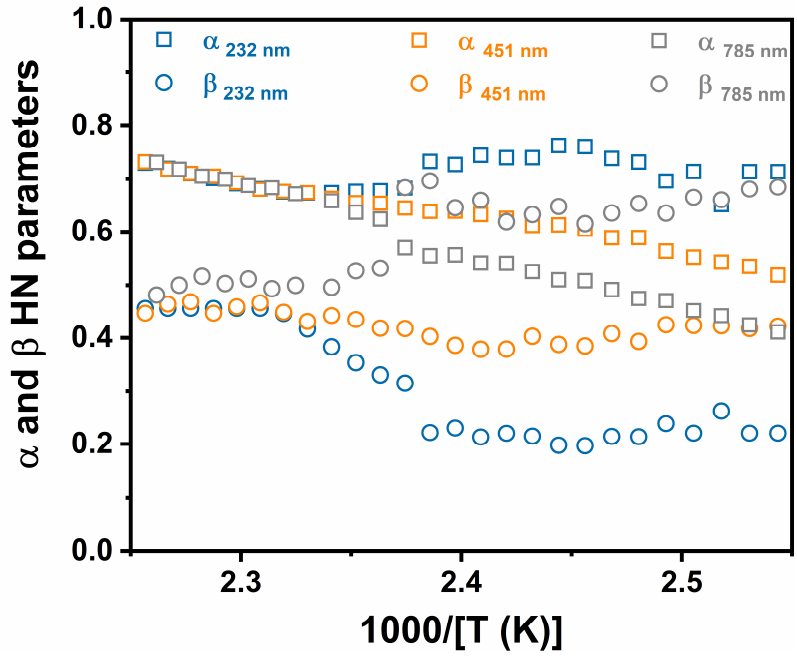

Figure 6. Fitting parameters α and β, obtained from Havriliak–Negami equation, versus inverse temperature for PAN_232, PAN_451, PAN_785.

In Figure 7, $\Delta\varepsilon$ is normalized to its maximum value, and plotted as a function of temperature for all the samples. This allows comparing directly the trend of the dielectric strength for each sample as a function of temperature. However, we do not recommend comparing the absolute value of the dielectric strength as the amount of air is influencing this value. The variation of the normalized dielectric strength with temperature follows a similar trend for all the samples and converges at high temperature. The expression of $\Delta\varepsilon$ is given by the Kirkwood–Fröhlich equation [51–52]:

$$\Delta\varepsilon = \frac{1}{3\varepsilon_0} g \frac{\mu^2}{k_B T} \frac{N}{V} \tag{5}$$

Where ε_0 is the vacuum permittivity, g is the Kirkwood correlation factor, μ^2 is the time–correlation function of the total dipole moment, k_B is Boltzmans's constant, T is the temperature, and N/V is the volume density of dipoles. While Eq. 5 shows that $\Delta\varepsilon$ is inversely proportional to the temperature, Figure 7 reveals in contrast that the dielectric strength monotonically increases with temperature. An overall increase in $\Delta\varepsilon$ might be related to an increase of the correlation factor (which is however known to be inversely dependent on the temperature), an increase in the dipole moment (which seems unlikely since all the fiber mats are made of PAN), or an increase in the density of dipoles N/V. The increase of N/V with temperature has previously been reported for semi–crystalline polymers [53] and is associated with the progressive mobilization of constrained amorphous phase which devitrifies in a temperature domain that is not limited to the calorimetric glass transition. For example this could indicate the presence of RAF in the material. Indeed RAF is the part of the amorphous phase that does not mobilize during the glass transition but devitrifies in a temperature domain, often broad, which stands above the glass transition. Electrospinning induces an orientation of the polymer chains. Thus, we hypothesize that this behavior is the signature of initial orientation, which severely constrains the mobility in the amorphous phase close to the calorimetric glass transition, but then progressively vanishes with the temperature increase due to polymer chain relaxation. Until merging of the curves, the dielectric strength is the lowest for PAN_232. This is consistent with the idea that polymer chains are more oriented in this sample.

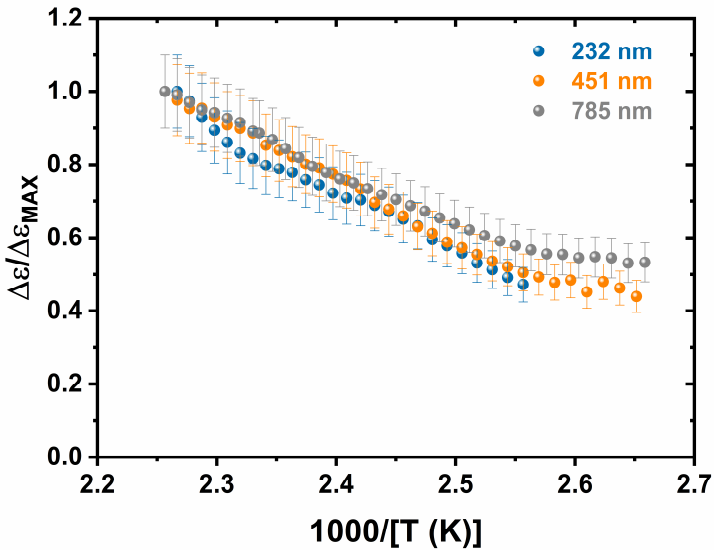

Figure 7. Evolution of the normalized dielectric strength with temperature obtained from DRS measurements for PAN_232, PAN_451, and PAN_785. The error bars were estimated as 10% of the recorded value.

In Figure 8a the relaxation time is plotted as a function of the inverse of temperature. As expected, the samples exhibit a non–linear dependence of the relaxation time with temperature, which is typical of the α–relaxation process associated with the glass transition. The Arrhenius plots were fitted with the Vogel–Tamman–Fulcher (VTF) law:

$$\tau = \tau_0 exp\left(\frac{DT_0}{T-T_0}\right) \tag{6}$$

Where τ_0 is a pre–exponential factor, D is a dimensionless parameter related to the slope variation (steepness strength), and T_0 is the Vogel temperature. VTF fitting parameters are given in Table 2.

Table 2. Fitting parameters of the VTF equation for PAN_232, PAN_451 and PAN_785 obtained from the combination of MT–DSC and DRS results (solid line).

	log τ_0	D	T_0
PAN_232	-10.5 ± 0.1	3.1 ± 0.1	321.2 ± 0.8
PAN_451	-10.9 ± 0.1	3.8 ± 0.1	314.0 ± 0.5
PAN_785	-11.0 ± 0.1	4.2 ± 0.2	307.5 ± 1.2

We observe a good concordance of the fits with, and without, adding the calorimetric glass transition data at the relaxation time corresponding to a period of 100s of MT–DSC analysis. At high temperature the relaxation time is the same for all materials, while the curves start deviating from each other with the decrease in temperature. PAN_232 exhibits the highest relaxation times close to the glass transition. From a T_g normalized representation of the relaxation time variations (Figure 8b), it is possible, as proposed by Angell [42], to compare the materials by the slope of the deviation from the Arrhenius behavior, using the fragility index *m*.

$$m = \left.\frac{dlog_{10}(\tau)}{d(T/T_g)}\right|_{T=T_g} \tag{7}$$

Despite the shift of the glass transition, PAN_451, and PAN_785 exhibit the same fragility index (about 100). On the other hand the slope is more steep for PAN_232 leading to a fragility index of 133. The uncertainties on kinetic fragility are about 10% of the calculated index (see Table 1).

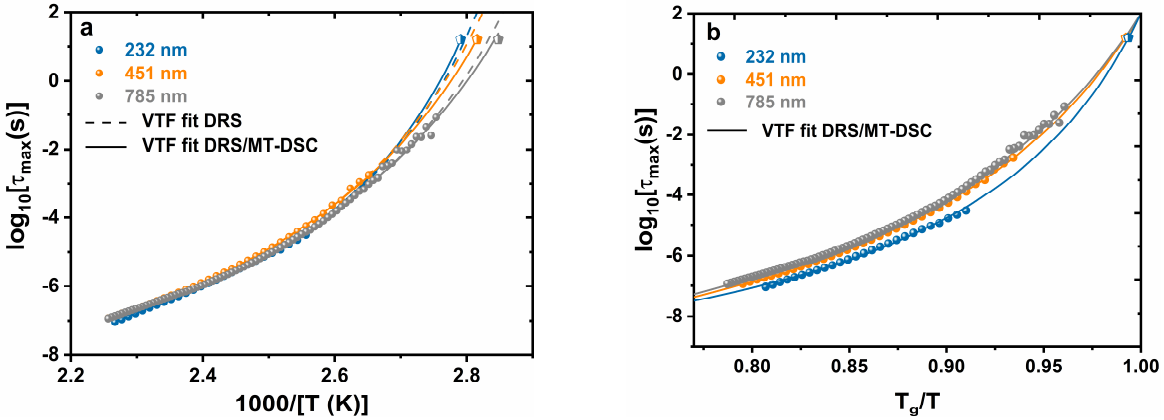

Figure 8. **(a)** Evolution of the relaxation time with the inverse of temperature from DRS measurements and **(b)** T_g normalized variations of the relaxation time for PAN_232, PAN_451, and PAN_785. Dashed curves correspond to VTF fit from DRS data and solid curves correspond to VTF fit from the combination of DRS and MT–DSC data.

According to the approach of Donth [54], the cooperativity length ξ can be calculated from the temperature fluctuation associated with the glass transition, which can be estimated from calorimetric measurements such as MT–DSC using Equation 8:

$$\xi_{T_\alpha}^3 = \frac{\left(\frac{1}{Cp_{glass\,T\alpha}} - \frac{1}{Cp_{liquid\,T\alpha}}\right) k_B T_\alpha^2}{\rho \delta T^2} \tag{8}$$

Where Cp is the specific heat capacity at constant pressure, k_B is the Boltzmann's constant, T_α is the dynamic glass transition temperature, ρ is the density equal to 1.2 [55], and δT is the mean square temperature fluctuation associated with the glass transition. The Cp glass and liquid values as well as the δT were extracted first by MT–DSC measurements from the calorimetric glass transition temperature for every sample. Values of ξ = 1.7 nm, 1.9 nm, and 2.1 nm were obtained for PAN_232, PAN_451, and PAN_785 respectively. Saiter *et al.* [56] proposed to extend the calculation of the cooperativity length from the calorimetric glass transition to the rise of cooperativity at the temperature of crossover, by combining DRS and MT–DSC measurements. To do so, δT was estimated as a function of temperature from DRS results. Cp glass was estimated as a function of temperature from the equation proposed by Gaur et al. [45]. Cp liquid was recorded as a function of temperature from MT–DSC measurements. Data are reported in the supporting information as Table SI.2, SI.3 and SI.4 for PAN_232, PAN_451 and PAN_ 785 respectively. As can be seen in Figure 9a, for temperatures significantly above the calorimetric glass transition, the cooperativity length is identical between samples. Moreover, the cooperativity decreases with the increase of temperature, consistently with previous studies [56–57]. The cooperativity is plotted in Figure 9b as a function of relaxation time.

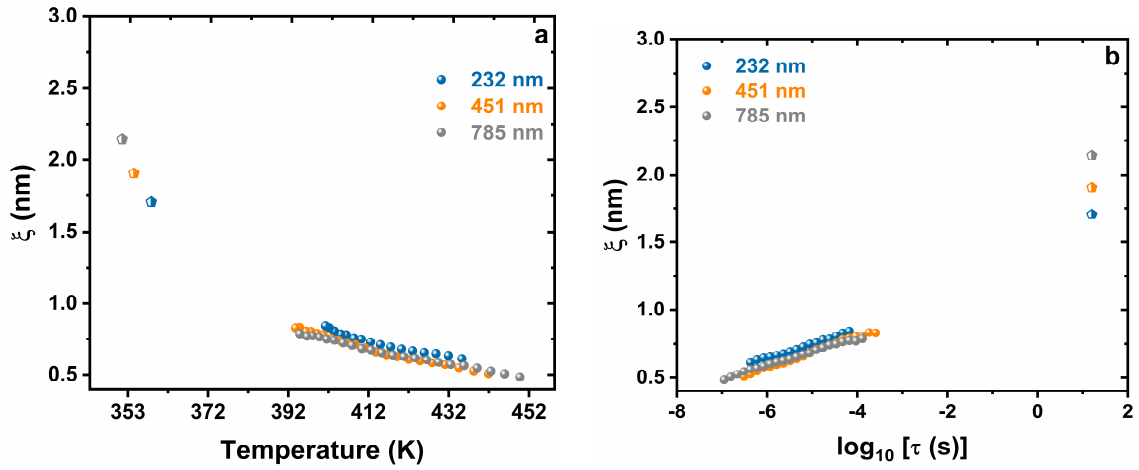

Figure 9. **(a)** Cooperativity length as a function of temperature, and **(b)** as a function of the relaxation time, calculated for PAN_232, PAN_451, and PAN_785.

For τ = 16 seconds, which corresponds to the calorimetric glass transition, cooperativity differs between the samples. ξ decreases with the fiber average diameter. A decrease of

cooperativity was previously reported when increasing the polymer chain orientation [34–38]. On the other hand, for lower relaxation times, the cooperativity is the same between PAN_232, PAN_451, and PAN_785. This again suggests that the relaxation dynamics are only influenced by orientation close to the calorimetric glass transition.

Hong *et al.* [58] separated the fragility index m in two contributions (see Eq. 9). The index m_V depicts the pure thermal variations of the relaxation time in isochoric conditions. Its counterpart (m - m_V) represents the fragility term that is sensitive to volume variations.

$$m = m_V + \frac{\Delta V^{\#}}{Ln(10)k_B}\frac{\alpha_T}{\kappa} \quad (9)$$

Where κ is the compressibility and α_T is the coefficient of thermal expansion of the supercooled liquid at T_g. The ratio α_T/κ goes from 0.5 to 3.0 MPa / K for a wide range of glass formers, and $\Delta V^{\#}$ is equal to 5% of the cooperativity volume. Therefore (m - m_V) depends on the cooperativity length. For an average value α_T/κ = 1.5 MPa / K, (m - m_V) = 9, 13, and 19 for PAN_232, PAN_451, and PAN_785 respectively were obtained. Thus PAN_451 and PAN_785 exhibit close values for m_V, 93 and 81 respectively, while m_V equal to 124, for PAN_232, is significantly higher. As shown in a previous study on plasticized polylactide [59], the variations of cooperativity and fragility are correlated under the condition that m_V almost remains invariant. On the other hand, relaxation parameters m and ξ can also exhibit opposite variations [36,60] like in the present study. By investigating the relaxation dynamics in interpenetrated networks [61], we recently gave a structural interpretation of each fragility contribution in polymers. (m - m_V), which follows cooperativity, depicts the level of interchain interactions, whereas m_V is a parameter characteristic of the backbone rigidity, increasing with intrachain interactions, that could develop during orientation. It is assumed that m_V is the highest for PAN_232 because the amorphous phase is more oriented in this sample. One can consider that in the present study m_V gives qualitative information regarding the degree of orientation in fiber mats. More generally, we observe that the average fiber diameter has a strong impact on several relaxation parameters obtained from thermal analysis. The combined use of MT–DSC and DRS is potentially interesting to supplement data obtained from spectroscopy techniques such as X–Ray diffraction.

CONCLUSION

Characterizing polymer chain orientation in electrospun fibers is of high interest since their outstanding mechanical properties result from a combination of low crystallinity and high polymer chain alignment. This study shows the possibility to obtain relative information, i.e., to compare electrospun fiber mats, by investigating the relaxation dynamics, from the combination of modulated temperature differential scanning calorimetry (MT–DSC) and dielectric relaxation spectroscopy (DRS). The mat with smaller average nanofiber diameter exhibits both a decrease of the cooperativity length at the calorimetric glass transition, and an increase of the thermal contribution of fragility. Our interpretation is that these results are caused by a constraining of amorphous phase dynamics and by an increase in the polymer chain rigidity respectively. The potential explanation that these results could be related to an increase of the degree of crystallinity is inconsistent with the experimental results since the material exhibiting the lowest cooperativity also has the highest content of amorphous phase relaxing at the glass transition. More probably the change in the glass transition dynamics is associated with a stronger polymer chain alignment. Moreover, the relaxation dynamics, investigated from DRS, merge far above the calorimetric glass transition but significantly below the melting domain, suggesting a constraint slackening in the amorphous phase when crossing the glass transition. These results are also consistent with the decrease in crystallinity for smaller average nanofiber diameters previously observed by X–Ray diffraction studies [29]. It is worth mentioning that the influence of the orientation on the relaxation dynamics is only detected for the mat with the smallest average fiber diameter. This result is in agreement with previous investigations [16] showing major improvements in mechanical properties for nanofibers with diameter below 250 nm.

ACKNOWLEDGEMENTS

Dimitry Papkov and Yuris Dzenis gratefully acknowledge partial support of this work by grants from ONR (N000141410663), NSF (DMR-1310534, CMMI-1463636), NIH (1R01HL125736-01), and NCESR.

REFERENCES

[1] N .Bhardwaj, S. C. Kundu. Electrospinning: A fascinating fiber fabrication technique. Biotechnol Adv. 28 (3) (2010) 325–347. doi:10.1016/j.biotechadv.2010.01.004.

[2] E. Ewaldz, and B. Brettmann. Molecular Interactions in Electrospinning: From Polymer Mixtures to Supramolecular Assemblies. ACS Appl. Polym. Mater. 1 (3) (2019) 298–308. doi:10.1021/acsapm.8b00073

[3] S. Agarwal, A. Greiner, J. H. Wendorff. Functional materials by electrospinning of polymers. Progress in Polymer Science 38 (6) (2013) 963–991. https://doi.org/10.1016/j.progpolymsci.2013.02.001

[4] T. Jiang, E. J. Carbone, K. W. –H. Lo, C. T. Laurencin. Electrospinning of polymer nanofibers for tissue regeneration. Progress in Polymer Science 46 (2015) 1–24. https://doi.org/10.1016/j.progpolymsci.2014.12.001

[5] J. Ding, J. Zhang, J. Li, D. Li, C. Xiao, H. Xiao, H. Yang, X. Zhuang, X. Chen. Electrospun polymer biomaterials. Progress in Polymer Science 90 (2019) 1–34. https://doi.org/10.1016/j.progpolymsci.2019.01.002

[6] Y. Liao, C. –H. Loh, M. Tian, R. Wang, A. G. Fane. Progress in electrospun polymeric nanofibrous membranes for water treatment: Fabrication, modification and applications. Progress in Polymer Science 77 (2018) 69–94. https://doi.org/10.1016/j.progpolymsci.2017.10.003

[7] M. Séon–Lutz, A. –C. Couffin, S. Vignoud, G. Schlatter, A. Hébraud. Electrospinning in water and in situ crosslinking of hyaluronic acid / cyclodextrin nanofibers: Towards wound dressing with controlled drug release. Carbohydrate Polymers 207 (2019) 276–287. https://doi.org/10.1016/j.carbpol.2018.11.085

[8] H. Xu, M. Yamamoto, H. Yamane. Melt electrospinning: Electrodynamics and spinnability. Polymer 132 (2017) 206–215. https://doi.org/10.1016/j.polymer.2017.11.006.

[9] M. Inagaki, Y. Yang, F. Kang. Carbon Nanofibers Prepared via Electrospinning. Advanced Materials 24 (19) (2012) 2547–2566. https://doi.org/10.1002/adma.201104940

[10] N. Govinna, I. Sadeghi, A. Asatekin, P. Cebe. Thermal properties and structure of electrospun blends of PVDF with a fluorinated copolymer. J. Polym. Sci., Part B: Polym. Phys. 57 (2019) 312–322. https://doi.org/10.1002/polb.24786

[11] G. Liao, S. Jiang, X. Xu, Y. Ke. Electrospun aligned PLLA/PCL/HA composite fibrous membranes and their in vitro degradation behaviors. Mater. Lett. 82 (2012) 159–162. doi:10.1016/j.matlet.2012.05.085.

[12] I. K. Kwon, S. Kidoaki, T. Matsuda. Electrospun nano– to microfiber fabrics made of biodegradable copolyesters: structural characteristics, mechanical properties and cell adhesion potential. Biomaterials 26 (2005) 3929–3939. doi:10.1016/j.biomaterials.2004.10.007.

[13] K. Yoon, K. Kim, X. Wang, D. Fang, B. S. Hsiao, B. Chu. High flux ultrafiltration membranes based on electrospun nanofibrous PAN scaffolds and chitosan coating. Polymer 47 (2006) 2434–2441. doi:10.1016/j.polymer.2006.01.042.

[14] A. Aydogdu, E. Yildiz, Z. Ayhan, Y. Aydogdu, G. Sumnu, S. Sahin. Nanostructured poly(lactic acid)/soy protein/HPMC films by electrospinning for potential applications in food industry. European Polymer Journal 112 (2019) 477–486. https://doi.org/10.1016/j.eurpolymj.2019.01.006

[15] W. Serrano, A. Meléndez, I. Ramos, N. J. Pinto. Electrospun composite poly(lactic acid)/polyaniline nanofibers from low concentrations in CHCl3: Making a biocompatible polyester electro–active. Polymer 55 (2014) 5727–5733. doi:10.1016/j.polymer.2014.09.015.

[16] D. Papkov,Y. Zou,M. N. Andalib, A. Goponenko, S. Z. D. Cheng, Y. A. Dzenis. Simultaneously Strong and Tough Ultrafine Continuous Nanofibers. ACS Nano 7 (4) (2013) 3324–3331. doi:10.1021/nn400028p

[17] X .Zong, K. Kim, D. Fang, S. Ran, B. S. Hsiao, B. Chu. Structure and process relationship of electrospun bioabsorbable nanofiber membranes. Polymer 43 (2002) 4403–4412. doi:10.1016/S0032-3861(02)00275-6.

[18] X.–F. Wu,Y. Salkovskiy, Y. A. Dzenis. Modeling of Solvent Evaporation from Polymer Jets in Electrospinning. Appl. Phys. Lett. 98 (22) (2011) 223108. https://doi.org/10.1063/1.3585148

[19] L. Liu, Y. Ren, Y. Li, Y. Liang. Effects of hard and soft components on the structure formation, crystallization behavior and mechanical properties of electrospun poly(l–lactic acid) nanofibers. Polymer 54 (2013) 5250–5256. doi:10.1016/j.polymer.2013.07.046.

[20] G. Stoclet, R. Seguela, J–M. Lefebvre, C. Rochas. New Insights on the Strain–Induced Mesophase of Poly(d,l–lactide): In Situ WAXS and DSC Study of the Thermo–Mechanical Stability. Macromolecules 43 (2010) 7228–7237. doi:10.1021/ma101430c.

[21] K. Wasanasuk, K. Tashiro. Structural Regularization in the Crystallization Process from the Glass or Melt of Poly(l–lactic Acid) Viewed from the Temperature–Dependent and Time–Resolved Measurements of FTIR and Wide–Angle/Small–Angle X–ray Scatterings. Macromolecules 44 (2011) 9650–9660. doi:10.1021/ma2017666.

[22] Y. Wang Y, H. Zhang, M. Li, W. Cao, C. Liu, C. Shen. Orientation and structural development of semicrystalline poly(lactic acid) under uniaxial drawing assessed by infrared spectroscopy and X–ray diffraction. Polym. Test. 41 (2015) 163–171. doi:10.1016/j.polymertesting.2014.11.010.

[23] Q. Ma, M. Pyda, B. Mao, P. Cebe. Relationship between the rigid amorphous phase and mesophase in electrospun fibers. Polymer 54 (2013) 2544–2554. doi:10.1016/j.polymer.2013.03.019.

[24] B. Wunderlich. Thermal Analysis of Polymeric Materials, Springer–Verlag, New York, 2005.

[25] H. Chen, P. Cebe. Vitrification and devitrification of rigid amorphous fraction of PET during quasi–isothermal cooling and heating. Macromolecules 42 (2009) 288–292. DOI: 10.1021/ma802104a

[26] B. Wunderlich. Reversible crystallization and the rigid–amorphous phase in semicrystalline macromolecules. Prog. Polym. Sci. 28 (2003) 383–450. https://doi.org/10.1016/S0079-6700(02)00085-0

[27] M. Richard–Lacroix, C. Pellerin. Molecular Orientation in Electrospun Fibers: From Mats to Single Fibers. Macromolecules 46 (24) (2013) 9473–9493. doi:10.1021/ma401681m

[28] D. Papkov, C. Pellerin, Y. A. Dzenis. Polarized Raman analysis of polymer chain orientation in ultrafine individual nanofibers with variable low crystallinity. Macromolecules 51 (2018) 8746−8751. DOI: 10.1021/acs.macromol.8b01869

[29] D. Papkov, N. Delpouve, L. Delbreilh, S. Araujo, T. Stockdale, S. Mamedov, K. Maleckis, Y. Zou, M. N. Andalib, E. Dargent, V. P. Dravid, M. V. Holt, C. Pellerin, Y. A. Dzenis. Quantifying Polymer Chain Orientation in Strong and Tough Nanofibers with Low Crystallinity: Toward Next Generation Nanostructured Superfibers. ACS Nano 13 (2019) 4893−4927. doi:10.1021/acsnano.8b08725

[30] G. Adam, J. H. Gibbs. On the Temperature Dependence of Cooperative Relaxation Properties in Glass–Forming Liquids. J. Chem. Phys. 43 (2004) 139–146. doi:10.1063/1.1696442.

[31] T. A. Tran, S. Said, Y. Grohens. Nanoscale characteristic length at the glass transition in confined syndiotactic poly(methyl methacrylate). Macromolecules 38 (2005) 3867−3871. DOI:10.1021/ma0487296

[32] K. Arabeche, L. Delbreilh, R. Adhikari, G. H. Michler, A. Hiltner, E. Baer, J.–M. Saiter. Study of the cooperativity at the glass transition temperature in PC/PMMA multilayered films: influence of thickness reduction from macro− to nanoscale. Polymer 53 (2012) 1355–1361. https://doi.org/10.1016/j.polymer.2012.01.045.

[33] C. Schick, E. Donth. Characteristic length of glass transition: experimental evidence. Phys. Scr. 43 (4) (1991) 423–439. https://doi.org/10.1088%2F0031-8949%2F43%2F4%2F010

[34] F. Hamonic, D. Prevosto, E. Dargent, A. Saiter. Contribution of chain alignment and crystallization in the evolution of cooperativity in drawn polymers. Polymer 55 (2014) 2882–2889. doi:10.1016/j.polymer.2014.04.030.

[35] Y. Furushima, K. Ishikiriyama, T. Higashioji. The characteristic length of cooperative rearranging region for uniaxial drawn poly(ethylene terephthalate) films. Polymer 54 (2013) 4078–4084. doi:10.1016/j.polymer.2013.06.030.

[36] N. Delpouve, L. Delbreilh, G. Stoclet, A. Saiter, E. Dargent. Structural Dependence of the Molecular Mobility in the Amorphous Fractions of Polylactide. Macromolecules 47 (2014) 5186–5197. doi:10.1021/ma500839p.

[37] N. Delpouve, C. Lixon, A. Saiter, E. Dargent, J. Grenet. Amorphous Phase Dynamics at the Glass Transition in Drawn Semi–Crystalline Polyester. J. Therm. Anal. Calorim. 97 (2) (2009) 541–546. https://doi.org/10.1007/s10973-008-9670-2

[38] C. Lixon, N. Delpouve, A. Saiter, E. Dargent, Y. Grohens. Evidence of Cooperative Rearranging Region Size Anisotropy for Drawn PET. Eur. Polym. J. 44 (11) (2008) 3377–3384. https://doi.org/10.1016/j.eurpolymj.2008.08.001

[39] X. Monnier, N. Delpouve, N. Basson, A. Guinault, S. Domenek, A. Saiter, P. E. Mallon, E. Dargent. Molecular Dynamics in Electrospun Amorphous Plasticized Polylactide Fibers. Polymer 73 (2015) 68–78. https://doi.org/10.1016/j.polymer.2015.07.047

[40] H. W. Cho, B. J. Sung. The glass transition and interfacial dynamics of single strand fibers of polymers. Soft Matter 13 (2017) 1190−1199. doi:10.1039/C6SM02468H

[41] A. Codou, M. Moncel, J. G. van Berkel, N. Guigo, N. Sbirrazzuoli. Glass transition dynamics and cooperativity length of poly(ethylene 2,5–furandicarboxylate) compared to poly(ethylene terephthalate). Phys. Chem. Chem. Phys. 18 (2016) 16647−16658. doi:10.1039/C6CP01227B

[42] C. A. Angell. Spectroscopy simulation and scattering, and the medium range order problem in glass J. Non–Cryst. Solids 73 (1985) 1−17. https://doi.org/10.1016/0022-3093(85)90334-5

[43] S. Havriliak, S. Negami. A complex plane analysis of α–dispersions in some polymer systems. J. Polym. Sci., Polym. Symp. 14 (1966) 99−117. https://doi.org/10.1002/polc.5070140111

[44] A. A. Lacey, D. M. Price, M. Reading. Theory and practice of modulated temperature differential scanning calorimetry. Modul. Temp. Differ. Scanning Calorim., Springer (2006) 1–81.

[45] U. Gaur, S–F Lau, B. B. Wunderlich, B. Wunderlich. Heat capacity and other thermodynamic properties of linear macromolecules VI. Acrylic polymers. Journal of Physical and Chemical Reference Data 11 (1982) 1065. https://doi.org/10.1063/1.555671

[46] B. Wunderlich. Heat capacities of solid polymers. The Advanced THermal Analysis System, ATHAS Conference Paper 1990.

[47] E. Hempel, G. Hempel, A. Hensel, C. Schick, E. Donth. Characteristic Length of Dynamic Glass Transition near Tg for a Wide Assortment of Glass–Forming Substances. J. Phys. Chem. B 104 (2000) 2460–2466. doi:10.1021/jp991153f.

[48] K. Takahashi, D. Sawai, T. Yokoyama, T. Kanamoto, S. H. Hyon. Crystal transformation from the α– to the β–form upon tensile drawing of poly(L–lactid acid). Polymer 45 (2004) 4969−4976. https://doi.org/10.1016/j.polymer.2004.03.108

[49] Y. Zhang, G. C. Rutledge. Electrical Conductivity of Electrospun Polyaniline and Polyaniline–Blend Fibers and Mats. Macromolecules 45 (2012) 4238−4246. https://doi.org/10.1021/ma3005982

[50] A. Schönhals, F. Kremer. Analysis of dielectric spectra, in: F. Kremer, A. Schönhals (Eds.) Broadband dielectric spectroscopy, Springer, Berlin, Heidelberg, 2003, pp. 59−98. https://doi.org/10.1007/978-3-642-56120-7_3

[51] C. J. F. Böttcher. Theory of electric polarization, vol. I. Dielectrics in static fields. 2nd Edition. Elsevier, Amsterdam, The Netherlands (1973).

[52] L. Onsager. Electric Moments of Molecules in Liquids. J. Am. Chem. Soc. 58 (1938) 1486–1493. doi: 10.1021/ja01299a050

[53] A. Esposito, N. Delpouve, V. Causin, A. Dhotel, L. Delbreilh, E. Dargent. From a Three–Phase Model to a Continuous Description of Molecular Mobility in Semicrystalline Poly(Hydroxybutyrate–Co –Hydroxyvalerate). Macromolecules 49 (13) (2016) 4850–4861. doi:10.1021/acs.macromol.6b00384

[54] E. Donth. The Size of Cooperatively Rearranging Regions at the Glass Transition. J. Non. Cryst. Solids 53 (3) (1982) 325–330. https://doi.org/10.1016/0022-3093(82)90089-8

[55] R. B. Hurley, L. S. Tzentis. Density of polyacrylonitrile. Polym. Lett. 1 (1963) 423−426. https://doi.org/10.1002/pol.1963.110010806

[56] A. Saiter, L. Delbreilh, H. Couderc, K. Arabeche, A. Schönhals, J–M. Saiter. Temperature dependence of the characteristic length scale for glassy dynamics: Combination of dielectric and specific heat spectroscopy. Phys. Rev. E 81 (2010) 041805. https://doi.org/10.1103/PhysRevE.81.041805

[57] B. Rijal, L. Delbreilh, A. Saiter. Dynamic heterogeneity and cooperative length scale at dynamic glass transition in glass forming liquids. Macromolecules 48 (22) (2015) 8219–8231. doi:10.1021/acs.macromol.5b01152

[58] L. Hong, V. N. Novikov, A. P. Sokolov. Is there a connection between fragility of glass forming systems and dynamic heterogeneity/cooperativity? J. Non–Cryst. Solids 357 (2) (2011) 351–356. https://doi.org/10.1016/j.jnoncrysol.2010.06.071

[59] S. Araujo, N. Delpouve, A. Dhotel, S. Domenek, A. Guinault, L. Delbreilh, E. Dargent. Reducing the gap between the activation energy measured in the liquid and the glassy states by adding a plasticizer to polylactide. ACS Omega 3 (12) (2018)17092–17099. doi: 10.1021/acsomega.8b02474

[60] M. Sharma, G. Madras, S. Bose. Unusual fragility and cooperativity in glass–forming and crystalline PVDF/PMMA blends in the presence of multiwall carbon nanotubes. Macromolecules 48 (8) (2015) 2740–2750. doi: 10.1021/acs.macromol.5b00418

[61] S. Araujo, F. Batteux, W. Li, L. Butterfield, N. Delpouve, A. Esposito, L. Tan, J.–M. Saiter, M. Negahban. A structural interpretation of the two components governing the kinetic fragility from the example of interpenetrated polymer networks. J. Polym. Sci. Part B Pol. Phys. 56 (20) (2018) 1393–1403. https://doi.org/10.1002/polb.24722

Electrospinning

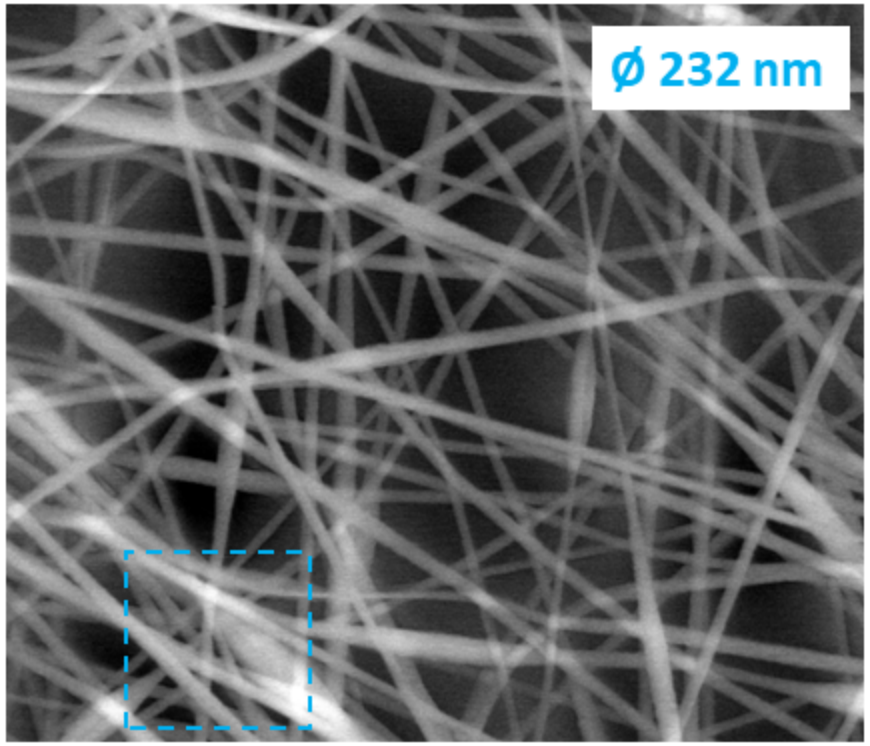

Relaxation dynamics

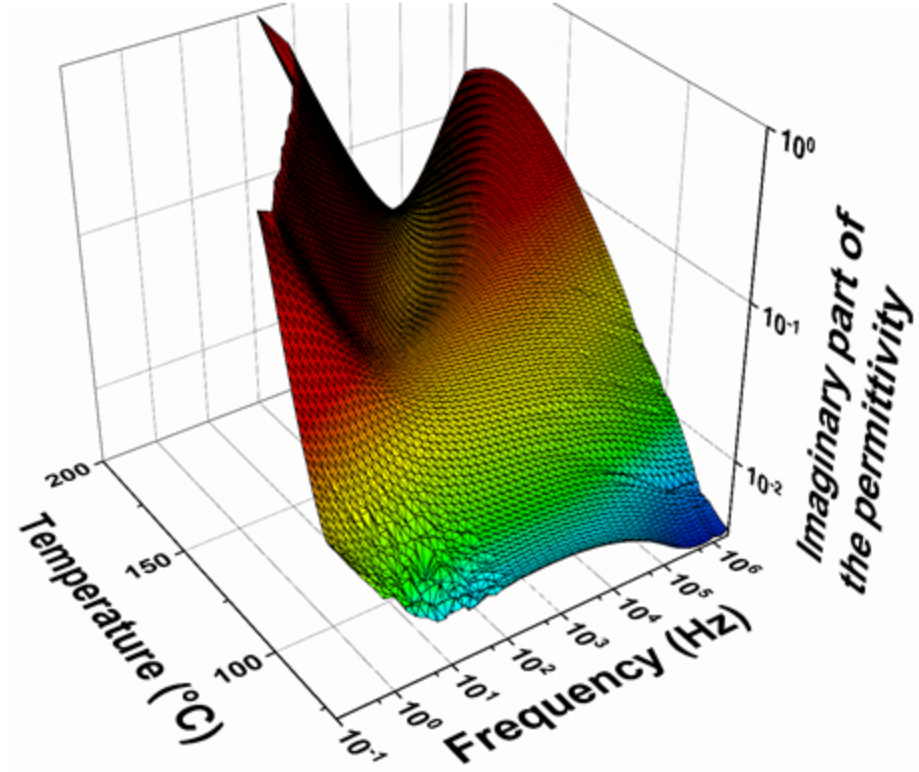

Structural interpretation

At T_g

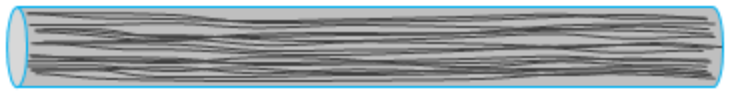

Well above T_g

Temperature